RSC Advances

PAPER

View Article Online
View Journal | View Issue



Cite this: *RSC Adv.*, 2025, **15**, 36924

# A high-performance magnetically separable and reusable $BiFeO_3/Bi_{25}FeO_{40}$ nano-photocatalyst for purifying water under visible light irradiation

Zahra Habibi Dehaghi,[a] Maryam Ghiyasiyan-Arani,*[a] Mehdi Shabani-Nooshabadi,*[a] Forat H. Alsultany[b] and Masoud Salavati-Niasari*[a]

Received 5th August 2025
Accepted 24th September 2025

DOI: 10.1039/d5ra05709d

rsc.li/rsc-advances

This research focuses on the rapid synthesis of photocatalyst materials based on bismuth iron oxides using the sol–gel technique in the presence of various saccharides. Bismuth iron oxides were used due to their magnetic properties and their band gaps that fall in the visible light region. The capacity of the synthesized samples to photodegrade and remove cationic and anionic dyes from water was evaluated. For the purposes of confirming the photocatalytic mechanism, a kinetic analysis and an examination of the active species were carried out. In addition, the recycling and reuse of the $BiFeO_3/Bi_{25}FeO_{40}$ nano-photocatalyst were investigated over a number of cycles. The $BiFeO_3/Bi_{25}FeO_{40}$ nanocomposite, which was synthesized in the presence of glucose, showed higher erythrosine photo-degradation efficiency, around 97% after 120 min under visible light irradiation, than the other samples. Also, after 5 cycles, the photo-degradation using the optimal catalyst reached 88% and it showed suitable stability.



## 1. Introduction

Uncontrolled pollution from industrial development of the air, water, and soil is a ticking time bomb that may permanently harm our surroundings and gravely endanger human life. We really have to move quickly to solve this issue before it is too late. Extensive studies have been conducted in this area as it is essential to solve the problem of wastewater contamination. Adsorption, biodegradation, reverse osmosis, flocculation, electrochemical oxidation, and photocatalysis are modern methods used for wastewater pollution removal and they provide a good path towards safer and cleaner environments.[1–3]

Improving the performance of photocatalysts depends on maximizing their efficiency. One efficient approach to doing this is by using morphologically well-organized photocatalysts. These structures improve electron transfer, optical absorption, and material photocatalytic activity.[4,5] One cannot ignore how crucial it is to obtain photocatalysts with well-structured morphologies. Without a well-organized framework, the photocatalyst will not operate at its optimum, which will lead to a subpar outcome. To guarantee the best potential outcomes, it is thus essential to concentrate on creating photocatalysts with well-ordered structures.[6,7] Photocatalysts are also essential for energy conversion and pollution purification. The design and fabrication of highly efficient photocatalysts will allow society to benefit from their advantages. Thus, a key first step in developing this technology is designing and manufacturing a highly efficient photocatalyst. An area of great research attention of late has been that of enhanced photocatalysts with great efficiency and stability improvement. Among other methods, the doping of elements, changing shapes, building heterogeneous structures, and the simultaneous loading of various catalysts have been investigated.[8] These techniques have resulted in encouraging outcomes and have significant power to transform photocatalytic processes.[9,10]

Improving the performance of many industrial activities depends on promoting the effectiveness of photocatalysts.[11] Nevertheless, the fast recombination of photogenerated electrons and holes usually reduces the individual photocatalyst performance. Building heterojunction photocatalysts has therefore been shown to be a successful approach for increasing photogenerated charge carrier transfer and separation, thereby suppressing recombination and obtaining high photocatalytic activity.[12,13] Designing photocatalysts requires making sure that the resulting product is extremely efficient, stable, and multifunctional. A semiconductor material leaves holes in its valence band when it is exposed to light with photon energies equal to or higher than its bandgap because the electrons in its valence band are excited and leap to the conduction band. Photogenerated electron–hole pairs are therefore produced. Many electrons and holes recombine during the migration process, however, because of defects and the coulombic force.[14] Few

[a]*Institute of Nano Science and Nano Technology, University of Kashan, Kashan 87317-51167, Islamic Republic of Iran. E-mail: m.ghiyasiyan@kashanu.ac.ir; m.shabani@kashanu.ac.ir; salavati@Kashanu.ac.ir; Fax: +98 31 55913201; Tel: +98 31 55912383*

[b]*Department of Medical Physics, College of Sciences, Al-Mustaqbal University, 51001, Babylon, Iraq*

electrons and holes go to the crystal surface and take part in the photocatalytic activity.[15]

Because of their layered structure, great stability, appropriate band gap, and strong catalytic activity, bismuth-based compounds are ideal for many uses.[16] These materials are also reasonably priced, which makes them perfect for anyone trying to optimize an investment.[17]

Bismuth ferrite ($BiFeO_3$) is one of the most researched magneto-electric multiferroic materials because it is the only single-phase material that displays simultaneous magnetic and ferroelectric ordering at ambient temperature.[18,19] $BiFeO_3$ is a "multiferroic-semiconductor" and its ferroelectricity-induced band-bending phenomena is a desirable trait that may fundamentally aid the photocatalytic process in numerous ways. As a "multiferroic-semiconductor," $BiFeO_3$ might open up new pathways for the photocatalysis sector and may be used as a next-generation material instead of the conventional semiconductors employed in present photocatalysts. Therefore, it is intriguing to examine the origin of the photocatalytic activity of $BiFeO_3$ from the standpoint of its ferroelectric and magnetic characteristics.[20] Although the individual merits of Bi-based oxides are often limited by factors such as the rapid recombination of photogenerated electron–hole pairs and suboptimal light harvesting, the sillenite-type structure of $Bi_{25}FeO_{40}$ offers active surface reaction sites for the adsorption and activation of organic pollutants.[21] One kind of sillenite material is $Bi_{25}FeO_{40}$. Using the top-seeded solution growth method, $Bi_{25}FeO_{40}$ single crystals can be created.[22] Iron sillenite has the structural formula $Bi_{12}(Bi_{1/2}Fe_{1/2})O_{19.5}$, with oxygen ions and cationic vacancies instead of $Bi^{5+}$ ions. A hydrothermal approach was used to create $Bi_{12}(Bi_{1/2}Fe_{1/2})O_{19.5}$ nanoparticles.[23–25]

Among the current nano-photocatalysts, magnetically recyclable nano-photocatalysts have demonstrated considerable promise for resolving recovery issues. Usually, magnetic nanoparticles coated with photocatalysts like ZnO and $TiO_2$ make up magnetically recyclable nano-photocatalysts. Magnetic materials like $ZnFe_2O_4$, $Fe_3O_4$, and $\gamma$-$Fe_2O_3$ impart the photocatalyst with magnetism that makes separation from the treated water simple. These magnetically recyclable nano-photocatalysts have demonstrated outstanding reusability and good efficiency in the breakdown of organic contaminants.[26] The advantages of magnetically recyclable nano-photocatalysts over traditional photocatalysts include easy recovery from the treated water, high scalability, improved reactivity for photocatalysis when using AOPs, and reduced material waste during application. The general trend of publications in the literature on magnetically recyclable nano-photocatalysts has been rising over the past ten years.[26,27]

Due to the superparamagnetic properties of bismuth iron oxides and their band gap of around 2 eV in the visible light range, this work is focused on the facile synthesis of $BiFeO_3$/$Bi_{25}FeO_{40}$-based photocatalyst materials through a sol–gel method in the presence of different saccharides. The photodegradation ability of the synthesized samples in terms of their removal of cationic (methyl violet) and anionic (erythrosine) dyes is compared. Kinetic studies and active species trapping investigations were conducted to confirm the photocatalytic mechanism. The active species trapping studies show that the photodegradation mechanism of erythrosine proceeds *via* hydroxyl radicals. Correspondingly, a pseudo-first-order kinetic model presents a direct relationship between the rate of photodegradation and the photodegradation efficiency. Also, recycling and reuse of the $BiFeO_3$/$Bi_{25}FeO_{40}$ nano-photocatalyst were examined over several cycles where the activity decreased by about 11%.

## 2. Experimental

### 2.1. Materials and equipment

Bismuth(III) nitrate pentahydrate, iron(III) nitrate nonahydrate, ethylene glycol, sucrose, glucose and starch, were among the chemical precursors and starting ingredients used in the production of the samples. These were acquired from Merck and used exactly as supplied, requiring no additional purification. All chemicals were of analytical grade and directly used in experiments.

The XRD patterns of the samples were obtained using a Philips X'pert Pro X-ray diffractometer with Ni-filtered Cu K$\alpha$ radiation (0.154 nm). The scan step size was 0.060° in continuous scan mode and the scan step time was 1.00° $min^{-1}$.

Fourier-transform infrared (FT-IR) spectra were obtained using a Nicolet Magna-550 spectrometer with KBr pellets.

Scanning electron microscopy (SEM) images were acquired using a MIRA3 TESKAN instrument equipped with energy dispersive X-ray spectroscopy. An EDX investigation was conducted using an accelerating voltage of 20 kV.

Transmission electron microscopy (TEM) images were acquired using a Philips EM208 transmission electron microscope at an accelerating voltage of 200 kV. The samples were dispersed in ethanol and drop-cast onto copper grids coated with a thin carbon film.

$N_2$ adsorption/desorption analysis (BET) was conducted at −196 °C utilizing an automated gas adsorption analyzer (Tristar 3000, Micromeritics). The pore size distribution was determined using the desorption branch of the isotherm *via* the Barrett, Joyner, and Halenda (BJH) technique.

Magnetic behavior was evaluated by means of a vibrating sample magnetometer (VSM, Meghnatis Kavir Kashan Co., Kashan, Iran).

The optical properties of the materials were investigated using ultraviolet-visible diffuse reflectance spectroscopy (UV-vis DRS) on a UNICO UV-1250 spectrophotometer from China. The diffuse reflectance spectra were recorded in the wavelength range of 200 to 1200 nm, and the Kubelka–Munk function was applied to convert the reflectance data into absorbance data.

### 2.2. Synthesis

In order to synthesis bismuth iron oxide (BF) nanostructures, a facile sol–gel procedure was used in the presence of diverse carbohydrates. The selected carbohydrates were glucose, sucrose and starch. 0.5 g of bismuth nitrate pentahydrate was dissolved in 10 mL of ethylene glycol and an aqueous solution of carbohydrate was added to the bismuth solution. Then, 0.41 g

of iron nitrate nonahydrate dissolved in ethylene glycol was mixed with the previous mixture. The resultant orange mixture was heated under constant stirring at 100 °C to form a gel. Finally, the dried gel was treated in a furnace (300 °C for 4 h and 600 °C for 2 h). The effect that the molar ratio of Bi : Fe and the effect that changing the carbohydrate fuel had on the synthesis of different phases of bismuth iron oxides are summarized in Table 1 and Scheme 1.

### 2.3. Photocatalytic setup

A pollutant model based on an aqueous solution of methyl violet and erythrosine with a specific concentration (5 ppm) was analyzed for photocatalytic activity for 120 minutes under a visible light. The lamp was used at a distance of 30 cm from the aqueous solution in a dark box (80 × 60 $cm^2$). The methyl violet and erythrosine solution was investigated by using a UV-vis spectrophotometer at wavelengths of 590 and 524 nm. The reactor was placed for 30 min in the dark box in order to make the photocatalyst particles adsorbed the maximum amount of dye molecules. After the adsorption state was achieved, the visible light irradiation was restarted to make the degradation reaction proceed. During the dye degradation process, a glass reactor (diameter = 4 cm, height = 6 cm) was used and the reactor was placed on a magnetic churn dasher. An OSRAM simulated sunlight source (irradiation power; 400 W, light intensity: 4000 lm, volts: 120 V, luminous flux: 2400 lm, wavelength: 400–700 nm) served as the light source. The suspension was then irradiated with visible light for a set irradiation time. Visible light irradiation of the reactor was done for 10, 20, 40, 60, 90, and 120 min. Continuous monitoring of the reaction was conducted by sampling for a specified duration time. The UV-vis spectrometer (UNICO spectrophotometer model UV2150) facilitated sampling over a designated time frame, and the absorbance of the samples was documented. Recovering the catalyst powder was conducted by centrifuging at 10 000 rpm for 5 min and repeating 3 times at each step. The efficiency of the degradation rate was determined using a formula that expresses the degradation rate relative to the time of irradiation. The percentage of pollutant degradation ($D$%) for a specified time can be calculated using the following equation:[1]

$$\text{Degradation } (D\%) = ((C_0 - C_t)/C_0) \times 100 \quad (1)$$

According to eqn (1), $D$ represents the percentage of degradation (%). $C_0$ and $C_t$ are the concentrations of the pollutants in the solution before and after degradation, respectively. The degradation rate was evaluated using the equation above.

## 3. Results

### 3.1. Crystalline phase purity

The effect that the molar ratio of Bi : Fe had on the phase purity of the sucrose-assisted sol–gel synthesized samples was examined using X-ray diffraction. According to Fig. 1a, synthesized sample (BF1) with a molar ratio of 1 : 1 (Bi : Fe) shows two phases, rhombohedral $BiFeO_3$ (JCPDS = 01-074-2016) and cubic $Bi_{25}FeO_{40}$ (JCPDS = 00-046-0416). Also, sample BF2 (Bi : Fe = 2 : 1) shows two phases of bismuth iron oxide including $BiFeO_3$ and $Bi_{25}FeO_{40}$. However by using a molar ratio of 1 : 2 (Bi : Fe) in the synthesis of sample BF3, three phases, $BiFeO_3$, $Bi_2Fe_4O_9$ and $Fe_2O_3$, can be observed (Fig. 1c). Reference codes of 00-025-0090 and 01-084-0309 matched with this pattern related to orthorhombic $Bi_2Fe_4O_9$ and $Fe_2O_3$, respectively. The effect that the carbohydrates had on the purity of the samples BF4 and BF5 is shown in Fig. 1d and e. Both samples show good matching with the $BiFeO_3$ and $Bi_{25}FeO_{40}$ phases.

The crystallite size was measured using the Scherrer equation and the derived data are summarized in Table 1. Also, derived data from the Scherrer equation were compared with the calculated data from the Williamson–Hall (W–H) plots for all samples (Fig. 2) in Table 1. According to the Williamson–Hall plot, $K\lambda/D$ is the intercept of the curve of $\beta\cos(\theta)$ *versus* $\sin(\theta)$. The equivalent values for $D$, $\lambda$, and $K$ are crystallite size, X-ray wavelength (0.154 nm for Cu), and the dimensionless form factor (about 0.9). As can be seen, the results indicate that the crystallite size as estimated by the Scherer equation is less than the crystallite size as determined by the Williamson–Hall plots for all samples because of the non-zero residual tension and positive slope of the W–H plots.[28]

The XRD reference intensity ratio (RIR) method determines phase weight fractions by comparing the relative diffraction intensities of phases in a mixture. It uses a known RIR value, generally from the ICDD's powder diffraction file (PDF) or experimental measurement, and the integrated intensity of a peak from a target phase in the mixture to compute the quantitative phase weight fraction value. When few calibration standard samples exist, this approach allows for the quick examination of multi-phase mixtures.

The basic equations connecting diffraction intensity ($I_i$) to concentration ($X_i$) should be followed by the main XRD

Table 1 Conditions for the synthesis of samples and XRD characterization data

| Sample no. | Fe : Bi | Fuel | Grain size[a] (nm) | Grain size[b] (nm) | Product | Phase percentage ratio[c] |
|---|---|---|---|---|---|---|
| BF1 | 1 : 1 (0.410 g : 0.500 g) | Sucrose (0.350 g) | 33.61 | 39.60 | $BiFeO_3/Bi_{25}FeO_{40}$ | 66% : 34% |
| BF2 | 1 : 2 (0.208 g : 0.500 g) | Sucrose (0.350 g) | 39.60 | 44.70 | $BiFeO_3/Bi_{25}FeO_{40}$ | 63% : 37% |
| BF3 | 2 : 1 (0.832 g : 0.500 g) | Sucrose (0.350 g) | 35.81 | 42.00 | $BiFeO_3/Bi_2Fe_4O_9/Fe_2O_3$ | 68% : 18% : 14% |
| BF4 | 1 : 2 (0.208 g : 0.500 g) | Glucose (0.204 g) | 37.44 | 49.50 | $BiFeO_3/Bi_{25}FeO_{40}$ | 54% : 46% |
| BF5 | 1 : 2 (0.208 g : 0.500 g) | Starch (0.500 g) | 36.28 | 47.79 | $BiFeO_3/Bi_{25}FeO_{40}$ | 66% : 34% |

[a] Scherrer Equation. [b] Williamson–Hall plot. [c] RIR method.

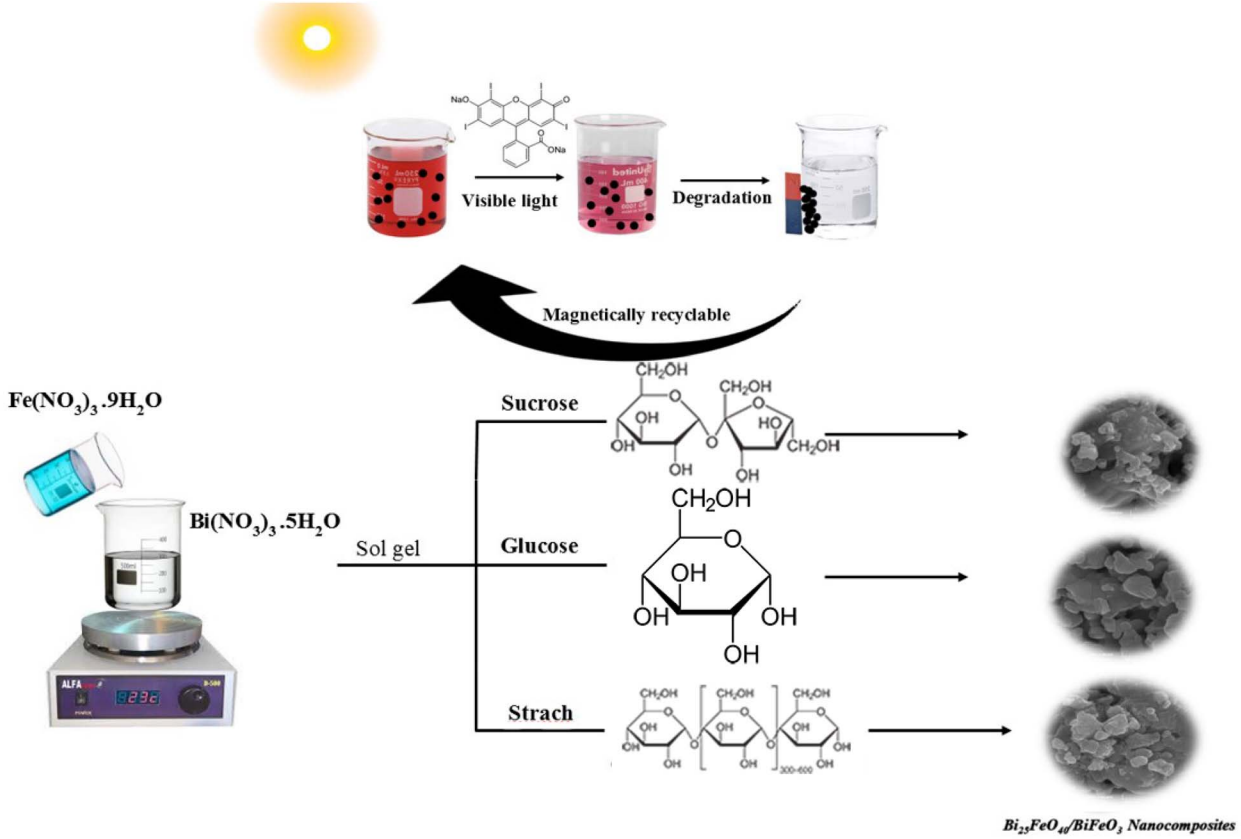


Scheme 1 Schematic diagram of the synthesis of magnetically separable and reusable $BiFeO_3/Bi_{25}FeO_{40}$ nanocomposites in the presence of different saccharides.

quantitative principle. Using a powder specimen, the RIR approach is as follows:

$$X_i = \frac{I_i}{\mathrm{RIR}_i} \times \left( \sum_{k=1}^{n} \frac{I_k}{\mathrm{RIR}_k} \right)^{-1} \quad (2)$$

where $I_i$ is the diffraction intensity or integral area of the diffraction peak, $\mathrm{RIR}_i$ is the RIR value, and $X_i$ is the weight percentage of the phase in the combination. When the RIR value is established, the quantitative result may be computed immediately using the intensities (integral area) of the strongest peaks, where the intensities are linked to peak height and FWHM.[29] The phase percentage ratio for each sample calculated using the RIR method are summarized in Table 1. Also, the phase percentage diagram can be seen in Fig. 1.

### 3.2. Morphology

All synthesized bismuth iron oxide samples were compared in terms of morphology and size using the FE-SEM images depicted in Fig. 3. The morphology of the samples with different molar ratios of precursors can be seen in Fig. 3a–c. Samples BF1 (Fig. 3a), BF2 (Fig. 3b) and BF3 (Fig. 3c) have agglomerated structures and were synthesized in the presence of sucrose carbohydrate as the fuel. However, glucose carbohydrate led to the formation of nanoparticles following the sol–gel synthesis of the BF4 sample (Fig. 3d). According to Fig. 3e, sample BF5 which was synthesized in the presence of starch shows an agglomerated structure. These results show that carbohydrates with massive structures led to agglomerated structures and the growth of crystals with large sizes. Starch polysaccharide with a polymeric structure and disaccharide sucrose could easily form hydrogen bonds with themselves and finally agglomerated products were obtained. But, using a monosaccharide carbohydrate like glucose with a small structure resulted in tiny and uniform nanoparticles.

Therefore, optimized sample is BF4 synthesized in the presence of glucose was studied using TEM at different magnifications to better understand its morphology. Fig. 4 shows TEM images of the BF4 sample where the presence of nanoparticles is seen.

### 3.3. Elemental and chemical structure

The EDS analysis of sample BF4 shows the presence of bismuth, iron and oxygen (Fig. 5a). In addition, there are not any impurities in this sample.

According to Fig. 5b, the FT-IR spectrum of sample BF4 confirms the presence of metal oxide chemical bonds in the range of 400–1000 $cm^{-1}$. Fe–O stretching vibrations are related to the absorption band at 812 $cm^{-1}$ and Bi–O stretching and deformation vibrations are attributed to the absorption bands

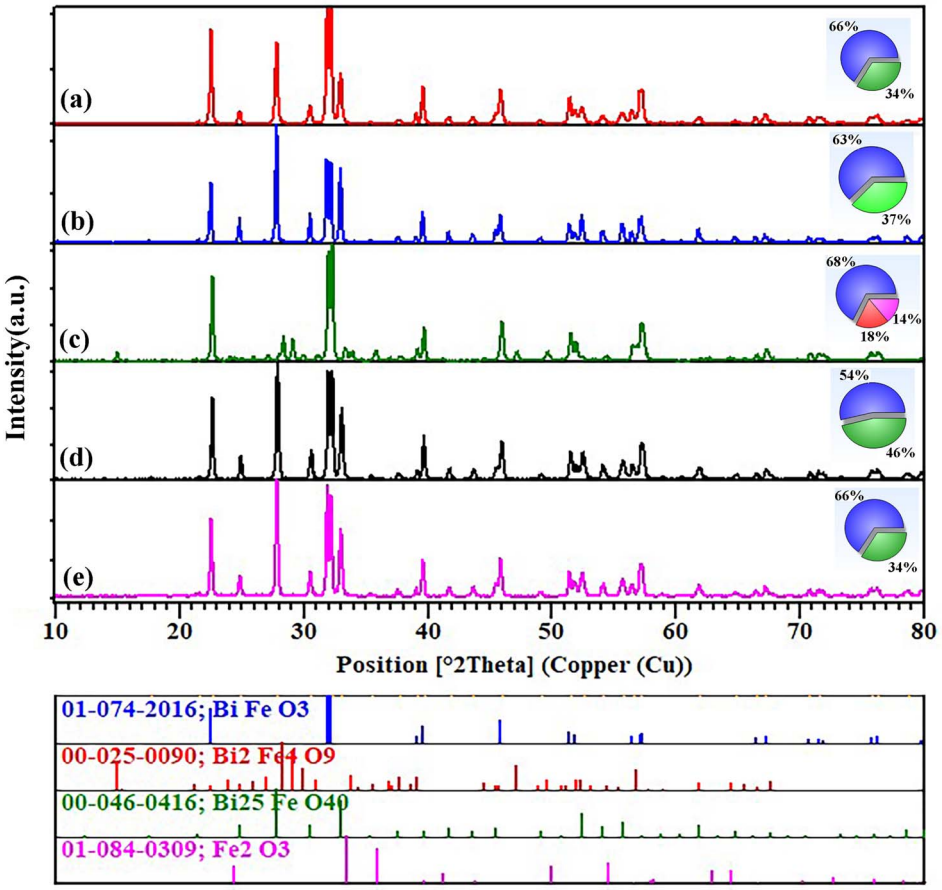


Fig. 1 XRD patterns of the synthesized samples (a) BF1, (b) BF2, (c) BF3, (d) BF4 and (e) BF5.

at 435 and 524 $cm^{-1}$. Therefore, this FT-IR analysis confirms the successful removal of the carbohydrates which were used as a fuel in the sol–gel synthesis.[30]

### 3.4. Surface area and magnetic behavior

The $N_2$ adsorption–desorption isotherms and the BJH pore size distribution of sample BF4 can be seen in Fig. 5c. According to the IUPAC classification, the produced isotherms show a type III hysteresis loop. This sample has a BET surface area and total pore volume of 11.376 $m^2 g^{-1}$ and 0.01736 $cm^3 g^{-1}$, respectively. The pore-size distribution shows the frequency of each pore size in a typical sample volume. The distribution of pore sizes in the sample underpins aggregation. Depending on the definition, the pore sizes can be macropores, micropores, and mesopores, which are intermediate-sized pores. The synthesized sample BF4 caused the average pore radius to expand to 6.105 nm.

The magnetic behavior of sample BF4 was studied by means of VSM hysteresis and the results are shown in Fig. 5d and e. The magnetic properties of the photocatalytic samples allow for easy separation from an aqueous medium. Based on the obtained hysteresis, sample BF4 shows superparamagnetic behavior with a saturation magnetization (Ms), retentive magnetization (Mr), and coercivity (Hc) of about 0.01684 emu $g^{-1}$, 0.001147 emu $g^{-1}$ and 51.5275 Oe, respectively. Thus, the $BiFeO_3/Bi_{25}FeO_{40}$ sample with superparamagnetic characteristics can be recycled with a magnetic field.

### 3.5. Optical properties

Selecting the best type of light source for photocatalytic degradation depends on knowing the band gap of the photocatalyst, a fundamental piece of knowledge. Comparing the $(KMh\nu)^n$ curve to zero $h\nu$ allowed us to determine the expected band gap for samples BF1, BF2, BF3, BF4 and BF5. Tauc's equation was used to determine the optical band gaps of the samples:

$$\alpha = \alpha_0(h\nu - E_g)^n/h\nu \quad (3)$$

In this context, $\alpha$ denotes the absorption coefficient; $h\nu$ denotes the photon energy; $\alpha_0$ and $h$ are constants; $E_g$ indicates the optical band gap of the material; $n$ depends on the type of electronic transition, assuming values between 1/2 and 3. A plot with $(\alpha h\nu)^{(1/n)}$ on the $y$-axis and $h\nu$ on the $x$-axis was created and a tangent to the linear region (orange line in Fig. 6) was drawn and extrapolated to the $x$-axis. The point where the tangent intersects the $x$-axis is the Tauc bandgap ($E_g$).

Fig. 6a show the relative UV-vis spectra for the resulting samples. The predicted band gaps of BF1, BF2, BF3, BF4 and BF5 are shown in Fig. 6b–f, respectively. The calculated band

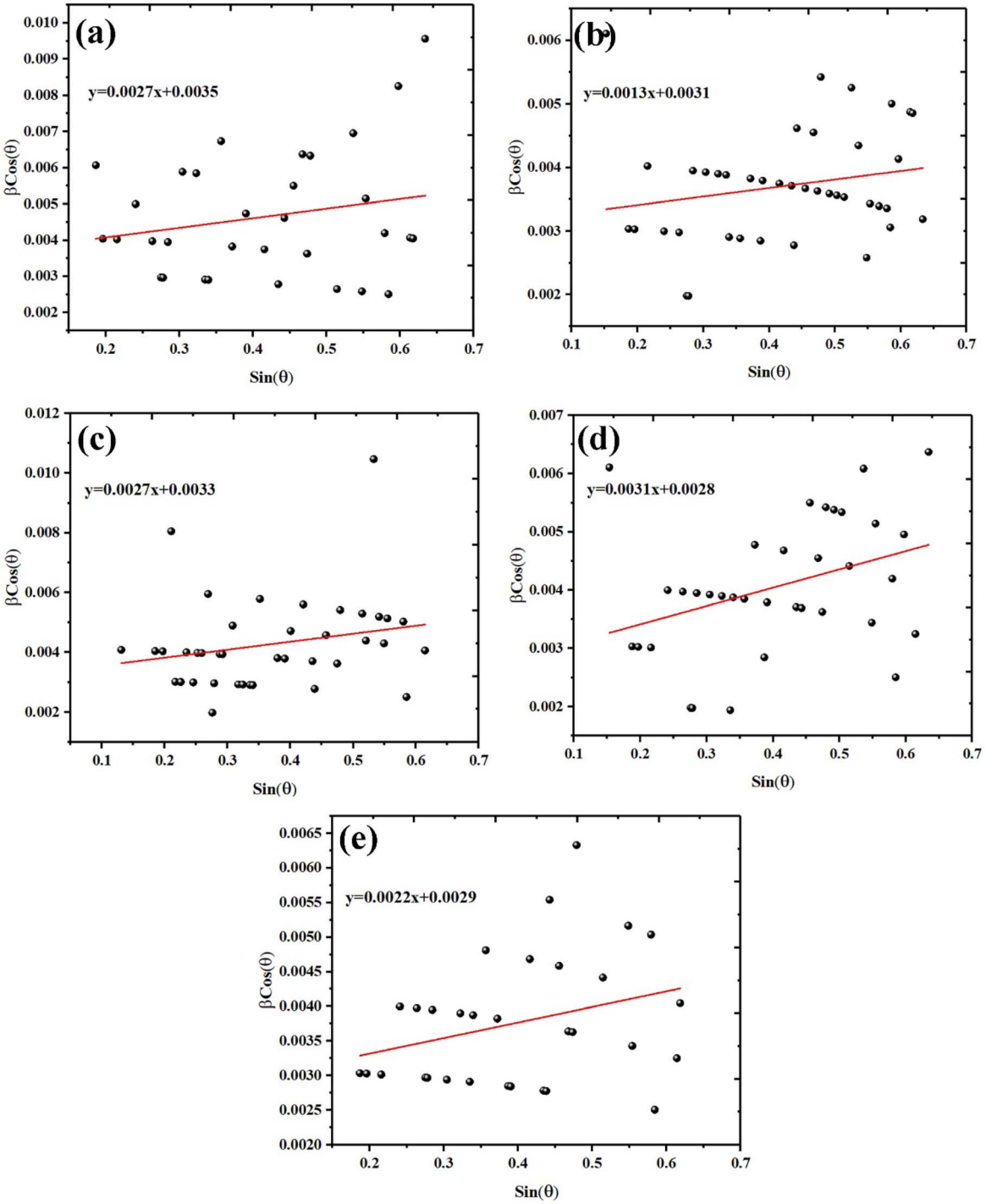


Fig. 2 Williamson–Hall plots for synthesized samples (a) BF1, (b) BF2, (c) BF3, (d) BF4 and (e) BF5.

gaps for samples BF1, BF2, BF3, BF4 and BF5 were 2.02 and 2.01, 1.99, 2.08 and 2.07 eV, correspondingly. All sample band gaps are in the visible range and they can all be used as photocatalysts under visible light irradiation.

### 3.6. Photocatalytic study

The photo-degradation efficiency of sample BF4 for anionic and cationic dyes was assessed. Erythrosine anionic dye and methyl violet cationic dye were selected as the model pollutants at a 5 ppm concentration. The visible light photocatalytic degradation of erythrosine and methyl violet in the presence of BF4 is shown in Fig. 7a and degradation percentages of 97.31% and 48.76% were reached after 120 min, respectively. Thus, erythrosine is an ideal model, as it shows higher degradation after 120 minutes, thus verifying that better efficiency was attained for the degradation of the anionic dye. The degradation of the

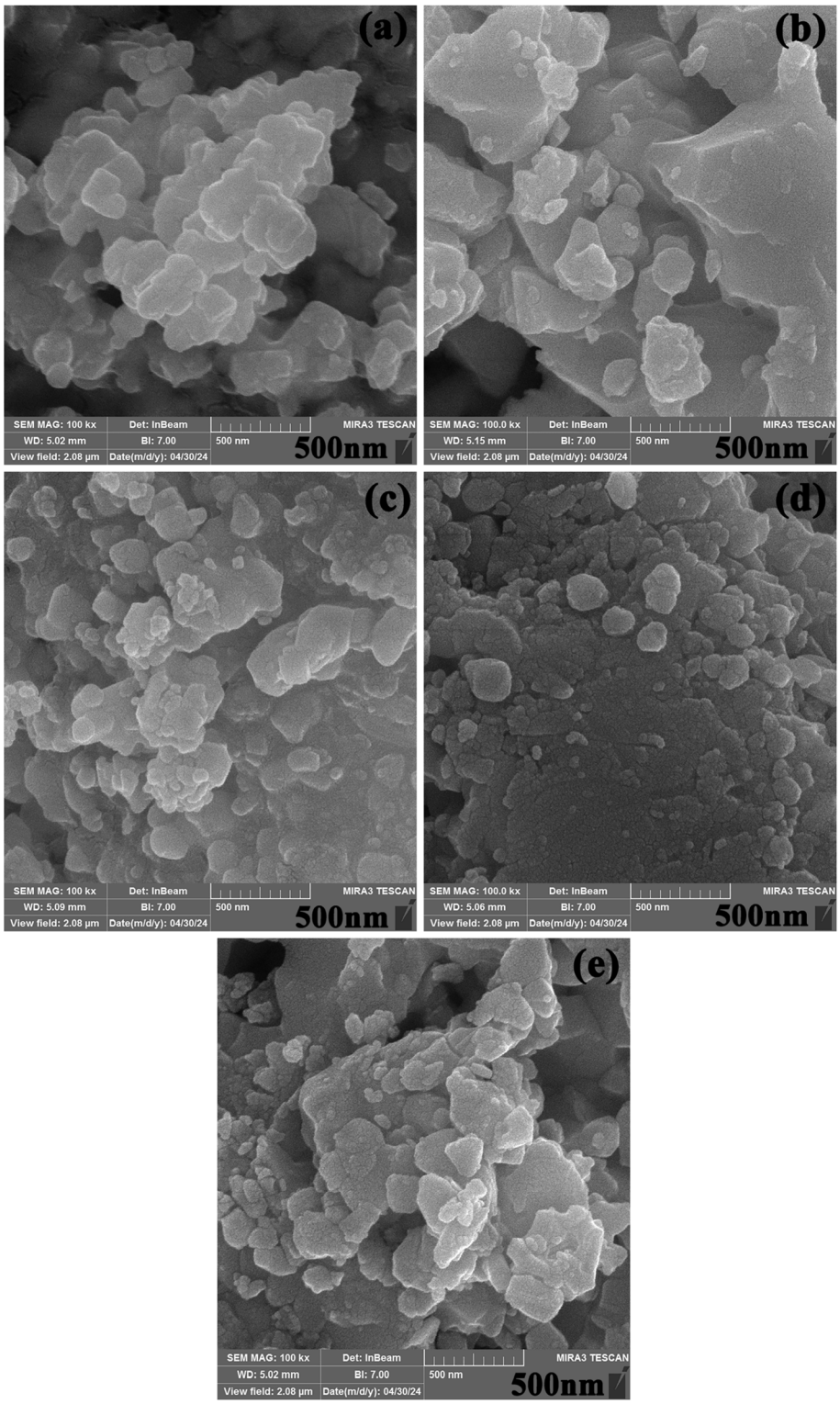


Fig. 3 FE-SEM images of synthesized samples (a) BF1, (b) BF2, (c) BF3, (d) BF4, and (e) BF5.

anionic dye (erythrosine) is more efficient than that of the cationic dye (methyl violet) due to the surface charge of the BF samples. So, adsorption of erythrosine on the surface of the BF sample is higher than that of methyl violet and led to effective interactions with the active sites.[31]

Numerous recent investigations have demonstrated that the kinetics of the decontamination of organic compounds follow a pseudo-first order kinetic model, which is compatible with the present work. The outstanding linear correlation between $-\ln(C/C_0)$ and irradiation time, where $C_0$ and $C$ are the

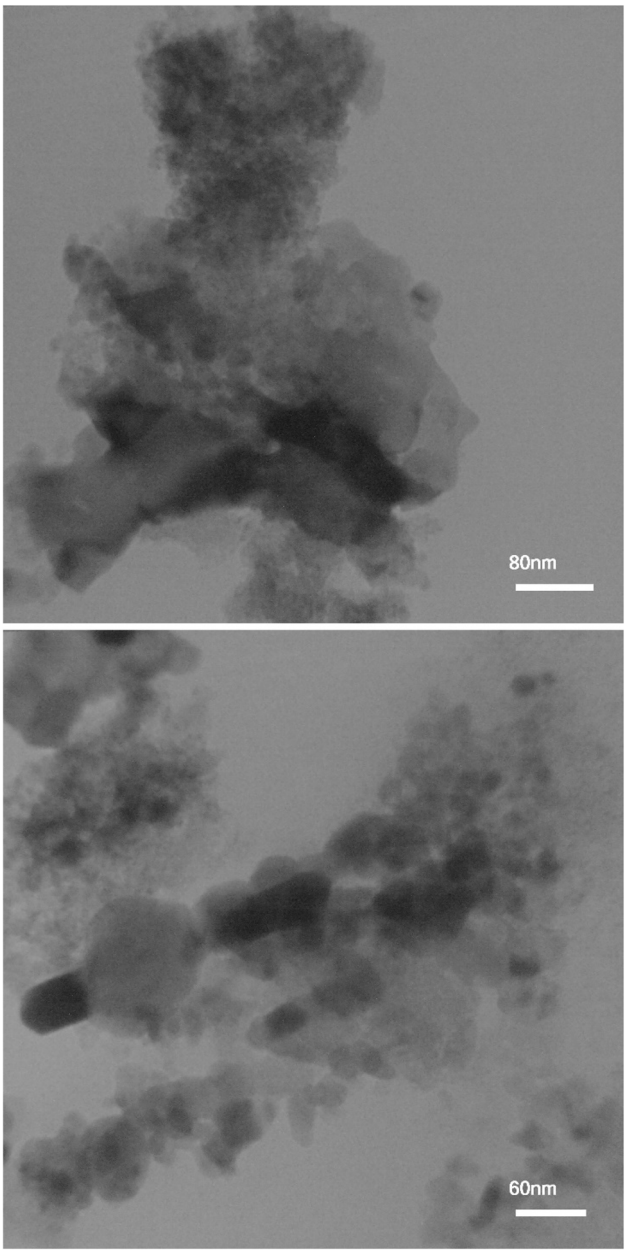


Fig. 4 TEM images of sample BF4.

pollution concentrations in the aqueous solution before and after degradation treatment time (t (min)), results in pseudo-first order degradation kinetics. It should be emphasized that the straight-line slope for a pseudo-first order process reflects $k$, the rate constant, which one may estimate with the formula $-\ln(C/C_0) = kt$.

The relationship between $-\ln(C/C_0)$ and time for the degradation of erythrosine and methyl violet in the presence of sample BF4 are shown in Fig. 7b and the rate constant was obtained from the slopes of these linear plots. For the photo-degradation of erythrosine and methyl violet, the apparent rate constants were 0.029 and 0.005 $min^{-1}$ respectively. These findings indicate that BF4 is more active for the photo-degradation of erythrosine than for the photo-degradation of methyl violet.

The photocatalytic activity and kinetics of samples BF1, BF2, BF3, BF4 and BF5 for the degradation of the optimized pollutant model (erythrosine) were compared, as depicted in Fig. 8a and b. The photo-degradation percentages of erythrosine by samples BF1, BF2, BF3, BF4 and BF5 were calculated to be 87.27%, 93.16%, 84.19%, 97.31%, and 73.01%, respectively. Also, the rate constant for these samples was measured as 0.016, 0.025, 0.022, 0.029, and 0.011 $min^{-1}$, respectively. A photolysis test under visible light irradiation in the absence of catalyst was conducted as a control test and 20.63% photodegradation of erythrosine was achieved.

The drop in the degradation by BF1 between 60 and 90 minutes can be caused by several photocatalytic phenomena. One common reason is the formation of stable intermediate products on the photocatalyst surface. These intermediates can temporarily be adsorbed on the active sites and reduce the access of active radicals ($^{\bullet}OH$ or $O_2^{\bullet-}$) to the main pollutant. During this time, due to the covering of the active sites or the competition of the intermediates with the main pollutant, the degradation rate decreases and there is a drop in the degradation curve. After a while (90 minutes), these adsorbed intermediates either decompose or are oxidized again to simpler molecules under the attack of active radicals and the photocatalyst surface is reactivated. This process causes the system to return to a stable degradation state and the curve increases. This behavior is observed in many photocatalytic systems and is called dynamic adsorption–desorption or competitive intermediate reactions. Therefore, the transient drop does not indicate photocatalyst deactivation, but rather a dynamic equilibrium between the formation and decomposition of intermediates during the reaction.[32–34]

Therefore, the optimized sample is BF4 which shows higher degradation efficiency than the other samples. Hence, the effect of catalyst loading was investigated to achieve the ideal conditions. Different catalyst dosages of 0.025, 0.050 and 0.075 g of sample BF4 were separately tested in 5 ppm erythrosine aqueous solution and the photo-degradation efficiency was studied. The degradation efficiency is shown in Fig. 8c and the rate constant for each test is compared in Fig. 8d. The photo-degradation of erythrosine in the presence of 0.025, 0.050 and 0.075 g of BF4 is about 91.79%, 97.31% and 95.96%, correspondingly. According to Fig. 8d, the rate constant for each test in the presence of 0.025, 0.050 and 0.075 g of sample BF4 were calculated to be 0.020, 0.029 and 0.023 $min^{-1}$, respectively.

The amount that each active agent contributes to the photocatalytic process is shown by the decrease in yield in the presence of scavengers. Fig. 9a shows the catalyst degradation efficiency in the presence of EDTA, isopropyl alcohol and benzoic acid. Scavengers such as EDTA, isopropyl alcohol, and benzoic acid may have varying effects on catalytic reactions, depending on the specific reaction and type of photocatalyst (Fig. 9a) being used. To investigate how sample BF4 degrades erythrosine, the $h^+$, $^{\bullet}O_2$, and $^{\bullet}OH$ active species were scavenged using EDTA, isopropyl alcohol, and benzoic acid, respectively.[35] The results of the scavenger tests showed that the addition of

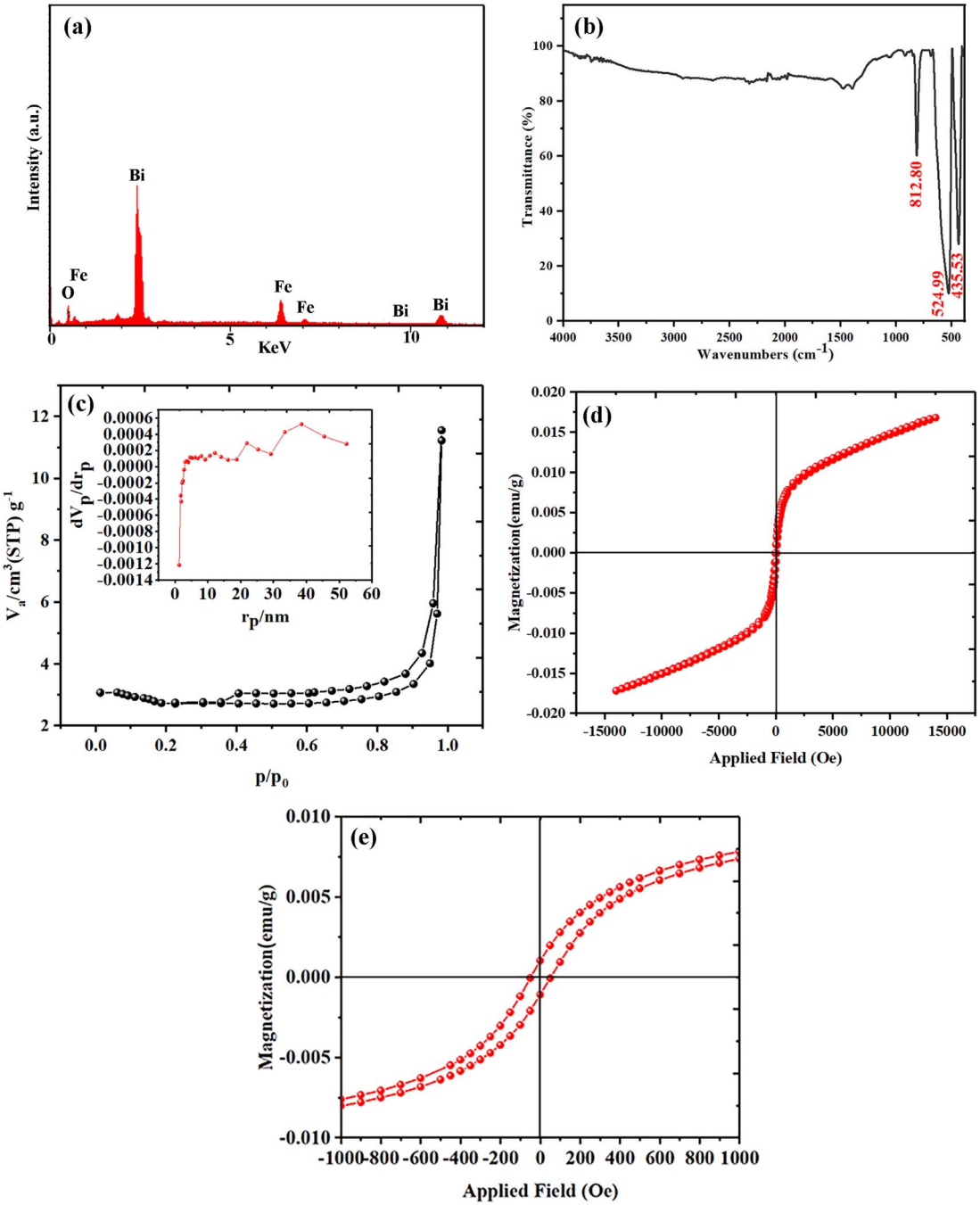


Fig. 5 (a) EDS analysis, (b) FT-IR analysis, (c) BET isotherm and BJH plot and (d and e) VSM hysteresis for sample BF4.

benzoic acid considerably reduced the rate of erythrosine degradation. Therefore, it is evident that hydroxyl radicals make up the majority of reactive species that produce the catalytic activity. Kinetic studies, which show a lower rate constant for the BF4 photocatalyst in the presence of benzoic acid compared to EDTA and isopropyl alcohol (Fig. 9b), support this finding.

The following is a potential mechanism for the photocatalytic enhancement as reported by A. Sun.[36] Our active species trapping experiments are in good agreement with the suggested photocatalytic process.

$$Bi_{25}FeO_{40}/BiFeO_3 + h\nu \rightarrow h^+ + e^- \quad (4)$$

$$H_2O + h^+ \rightarrow {}^{\cdot}OH + H^+ \quad (5)$$

$$OH^- + h^+ \rightarrow {}^{\cdot}OH \quad (6)$$

$$O_2 + e^- \rightarrow {}^{\cdot}O_2^- \quad (7)$$

$${}^{\cdot}OH + \text{erythrosine} \rightarrow H_2O + CO_2 \quad (8)$$

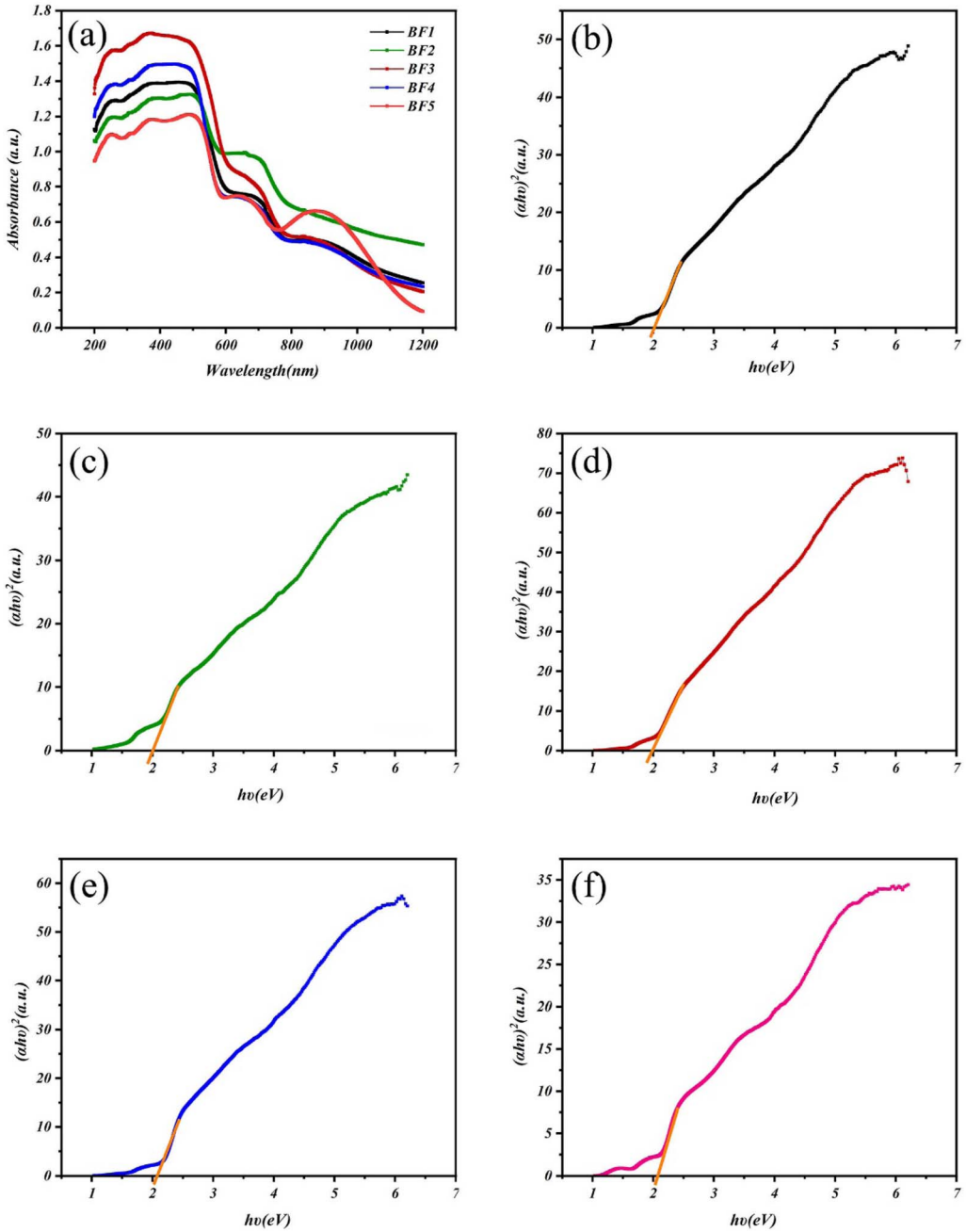


Fig. 6 Comparison of the (a) UV-vis spectra and plots of $(\alpha h\nu)^2$ *versus* $(h\nu)$ for samples (b) BF1, (c) BF2, (d) BF3, (e) BF4 and (f) BF5.

It is crucial to assess the catalytic stability of the photocatalyst study across a number of degradation cycles. Five iterations of repeated test cycles were carried out to remove erythrosine (5 ppm) using the 0.05 g of the BF4 catalyst in order to evaluate its stability. No discernible loss in activity happens after five iterations, as seen in Fig. 10. However, the small decrease in the degradation percentage observed may be explained by partial catalyst deactivation brought on by several reuses and photocatalyst loss during recovery. Based on Fig. 10, the catalytic efficiency loss for the photocatalyst recycling tests was estimated to be approximately 10.58%. The findings showed that BF4 was still recyclable and effective in breaking down contaminants even after many wastewater treatment cycles.

## 4. Conclusions

Different phases of bismuth iron oxides were synthesized using a sol–gel method in the presence of a diverse array of saccharides. Starch polysaccharide with a polymeric structure and the disaccharide sucrose could easily form hydrogen bonds with each other and therefore produce agglomerated products. However, glucose, a monosaccharide carbohydrate with a small structure, produced tiny and uniform nanoparticles. Therefore,

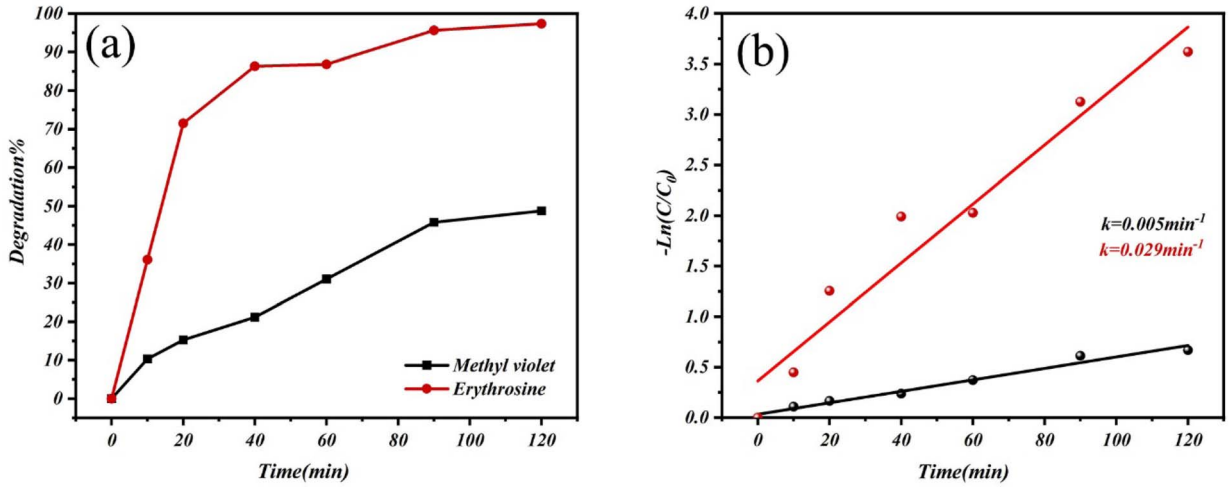


Fig. 7 (a) Photo-degradation of anionic and cationic dyes in the presence of the BF4 catalyst and (b) the relative plots of first-order degradation.

sample BF4 synthesized in the presence of glucose was selected as the optimal catalyst. The application of bismuth iron oxides was chosen because of their band gap in the visible light range of ~2 eV and their magnetic properties. The synthesized $BiFeO_3/Bi_{25}FeO_{40}$ sample shows high efficiency (97%) for the removal of the erythrosine anionic dye under visible light

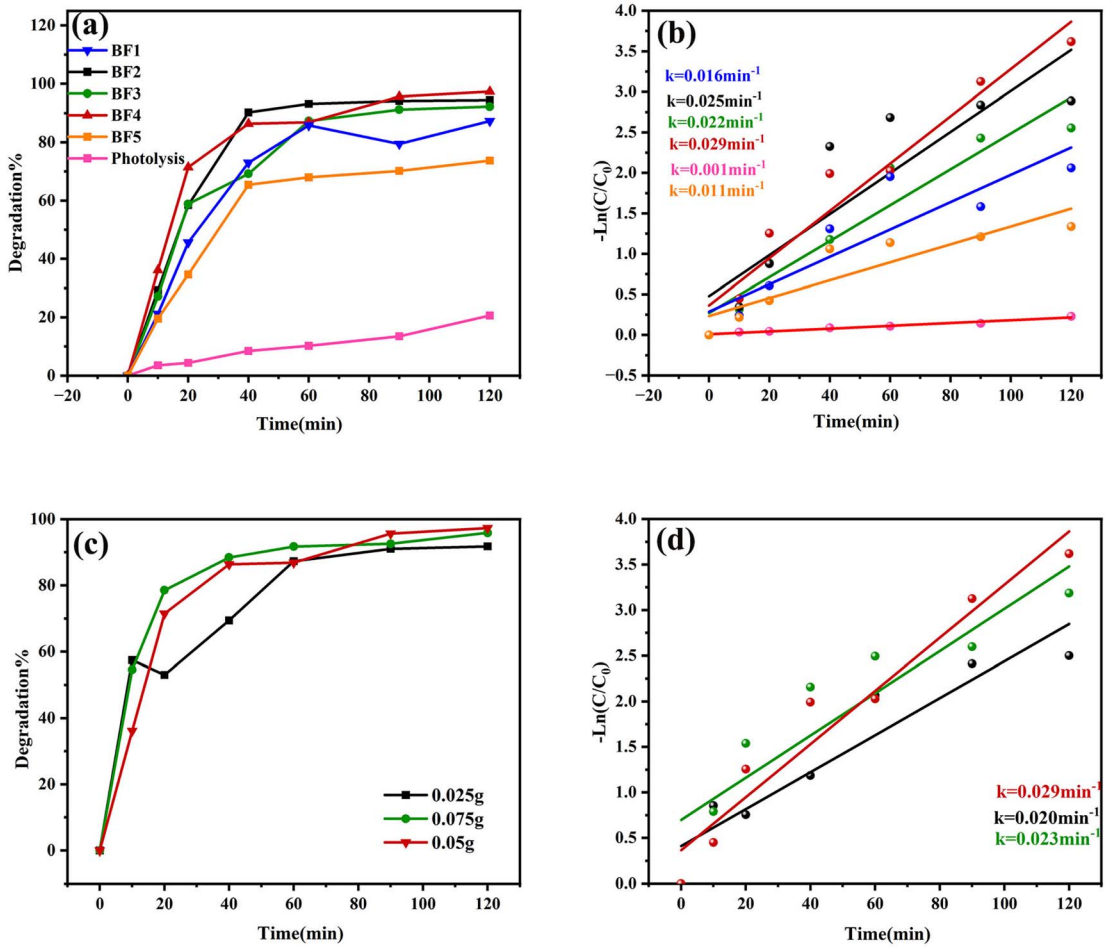


Fig. 8 (a and b) Photo-degradation of erythrosine in the presence of different synthesized catalyst and relative plots of first-order degradation. (c and d) Photo-degradation of erythrosine in the presence of different quantities of the BF4 catalyst and relative plots of first-order degradation.

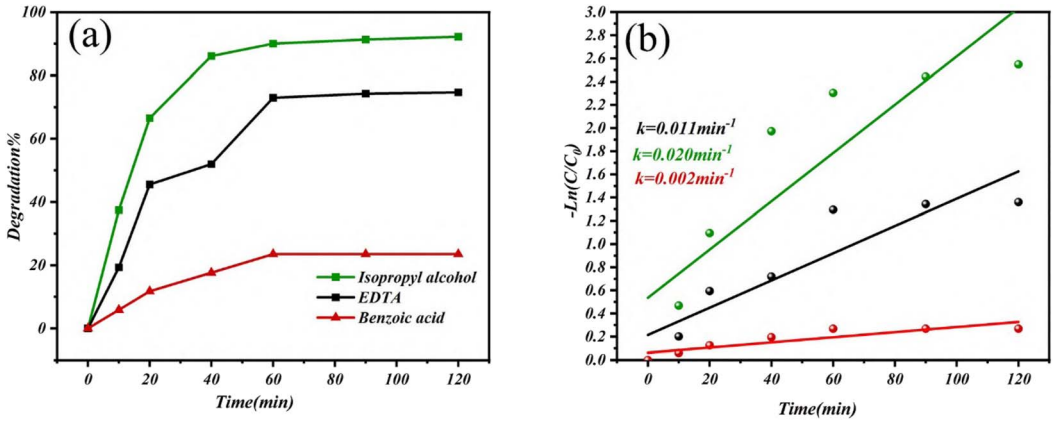


Fig. 9 (a) Mechanistic study of erythrosine degradation in the presence of the BF4 sample using different scavengers and (b) the relative plots of first-order degradation.

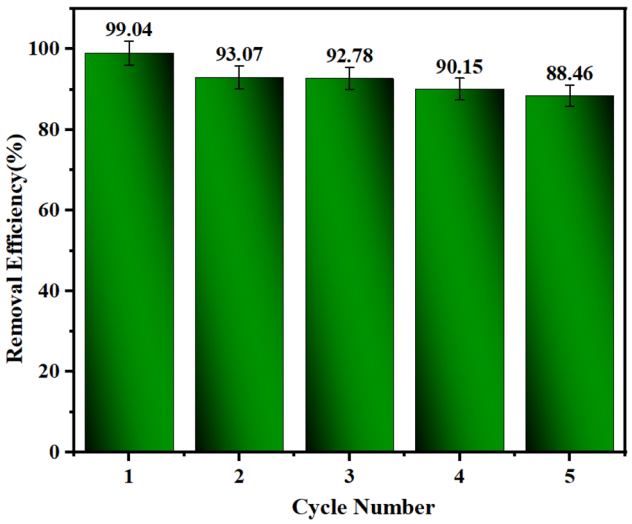


Fig. 10 Erythrosine photo-degradation using sample BF4 over successive cycles.

irradiation over 120 min. A kinetic study and a trapping investigation of the active species were performed in order to understand the photocatalytic process. Furthermore, the recycling and reuse of the $BiFeO_3/Bi_{25}FeO_{40}$ nano-photocatalyst over many cycles were explored and the photo-degradation reached 88% with sufficient stability noted after five cycles.

## Conflicts of interest

The authors declare that there are no conflicts of interest regarding the publication of this manuscript.

## Data availability

The authors confirm that the data supporting the findings of this study are available within the article. Additional data are available from the corresponding author upon reasonable request.

## Acknowledgements

The authors are grateful to the council of the University of Kashan for supporting this work through grants 159271/ZH1 and 1392548 and the Iran National Science Foundation: INSF (4032427).

## References

1 N. Yahya, F. Aziz, N. Jamaludin, M. Mutalib, A. Ismail, W. Salleh, *et al.*, A review of integrated photocatalyst adsorbents for wastewater treatment, *J. Environ. Chem. Eng.*, 2018, **6**, 7411–7425.
2 W. S. Koe, J. W. Lee, W. C. Chong, Y. L. Pang and L. C. Sim, An overview of photocatalytic degradation: photocatalysts, mechanisms, and development of photocatalytic membrane, *Environ. Sci. Pollut. Res.*, 2020, **27**, 2522–2565.
3 S. Begum and M. Ahmaruzzaman, CTAB and SDS assisted facile fabrication of SnO2 nanoparticles for effective degradation of carbamazepine from aqueous phase: a systematic and comparative study of their degradation performance, *Water Res.*, 2018, **129**, 470–485.
4 S. Iqbal, J. Liu, H. Ma, W. Liu, S. Zuo, Y. Yu, *et al.*, Development of TiO2 decorated Fe2O3QDs/g-C3N4 Ternary Z-scheme photocatalyst involving the investigation of phase analysis via strain mapping and its photocatalytic performance under visible light illumination, *Res. Chem. Intermed.*, 2023, **49**, 3327–3362.
5 R. R. Ikreedeegh, M. A. Hossen, M. Tahir and A. Abd Aziz, A comprehensive review on anodic TiO2 nanotube arrays (TNTAs) and their composite photocatalysts for environmental and energy applications: Fundamentals, recent advances and applications, *Coord. Chem. Rev.*, 2024, **499**, 215495.
6 H. Li, Y. Sun, Z. Y. Yuan, Y. P. Zhu and T. Y. Ma, Titanium phosphonate based metal–organic frameworks with hierarchical porosity for enhanced photocatalytic hydrogen evolution, *Angew. Chem., Int. Ed.*, 2018, **57**, 3222–3227.

7 J. You, Y. Zhao, L. Wang and W. Bao, Recent developments in the photocatalytic applications of covalent organic frameworks: A review, *J. Cleaner Prod.*, 2021, **291**, 125822.
8 T. Di, Q. Deng, G. Wang, S. Wang, L. Wang and Y. Ma, Photodeposition of CoOx and MoS2 on CdS as dual cocatalysts for photocatalytic H2 production, *J. Mater. Sci. Technol.*, 2022, **124**, 209–216.
9 A. Dey and P. R. Gogate, Chapter 24 – Nanocomposite photocatalysts-based wastewater treatment, in *Handbook of Nanomaterials for Wastewater Treatment*, ed. Bhanvase B., Sonawane S., Pawade V. and Pandit A., Elsevier, 2021, pp. 779–809.
10 M. Ahtasham Iqbal, S. Akram, S. khalid, B. Lal, S. U. Hassan, R. Ashraf, *et al.*, Advanced photocatalysis as a viable and sustainable wastewater treatment process: A comprehensive review, *Environ. Res.*, 2024, **253**, 118947.
11 W. Yu, M. H. Richter, P. Buabthong, I. A. Moreno-Hernandez, C. G. Read, E. Simonoff, *et al.*, Investigations of the stability of etched or platinized p-InP (100) photocathodes for solar-driven hydrogen evolution in acidic or alkaline aqueous electrolytes, *Energy Environ. Sci.*, 2021, **14**, 6007–6020.
12 J. Yu, L. Zhang, L. Wang and B. Zhu, *S-Scheme Heterojunction Photocatalysts: Fundamentals and Applications*, Elsevier, 2023.
13 L. Wang, X. Zheng, L. Chen, Y. Xiong and H. Xu, Van der Waals heterostructures comprised of ultrathin polymer nanosheets for efficient Z-scheme overall water splitting, *Angew. Chem., Int. Ed.*, 2018, **57**, 3454–3458.
14 J. Wang, W. Liao, Y. Tan, O. Henrotte, Y. Kang, K. Liu, *et al.*, Transfer dynamics of photo-generated carriers in catalysis, *Chem. Soc. Rev.*, 2025, **54**, 6553–6596.
15 F. Zhang, X. Xiao and Y. Xiao, In situ fabrication of type II 3D hierarchical flower-like BiOBr/Bi3O4Br heterojunction with improved photocatalytic activity, *J. Alloys Compd.*, 2022, **923**, 166417.
16 L. Chen, B. Guan, J. Guo, Y. Chen, Z. Ma, J. Chen, *et al.*, Review on the preparation and performance improvement methods of bismuth photocatalyst materials, *Catal. Sci. Technol.*, 2023, **13**, 5478–5529.
17 L. Wang, L. Wang, Y. Du, X. Xu and S. X. Dou, Progress and perspectives of bismuth oxyhalides in catalytic applications, *Mater. Today Phys.*, 2021, **16**, 100294.
18 J. Rout and R. N. P. Choudhary, Structural, electrical and magnetic behavior of mechanothermally synthesized multidoped bismuth ferrite, *Ceram. Int.*, 2018, **44**, 11543–11553.
19 A. Jain, Y. G. Wang, A. Kumar, N. Gupta, K. Kumar and A. K. Goyal, BiFeO3-based lead-free materials: Recent breakthroughs and their multifunctional applications, *J. Alloys Compd.*, 2025, **1010**, 177170.
20 M. Verma, A. Kumar, V. K. Thakur, A. Maurya, S. Kumar, S. Singh, *et al.*, Efficient and rapid sunlight-driven photocatalytic degradation of methylene blue dye using multiferroic BiFeO3 nanoparticles, *J. Sol-Gel Sci. Technol.*, 2025, **113**, 356–373.
21 Y.-J. Song, X.-Y. Bi, P. Xia, F. Sun, Z.-X. Chen, X.-Y. Zhang, *et al.*, A Simple One-Pot Method for the Synthesis of BiFeO3/Bi25FeO40 Heterojunction for High-Performance Photocatalytic Degradation Applications, *Int. J. Mol. Sci.*, 2024, **26**, 196.
22 M. T. Borowiec, A. Majchrowski, J. Zmija, H. Szymczak, T. Zayarniuk, E. Michalski, *et al.*, Crystal growth and optical properties of iron sillenite $Bi_{25}FeO_{40}$, *Solid State Crystals 2002: Crystalline Materials for Optoelectronics*, 2003, vol. 5136, pp. 26–30.
23 C. Zhang, H. Sun, W. Chen, J. Zhou, B. Li and Y. Wang, Hydrothermal synthesis and photo-catalytic Property of Bi 25 FeO 40 powders, *2009 18th IEEE International Symposium on the Applications of Ferroelectrics*, IEEE, 2009, pp. 1–3.
24 M. Valant and D. Suvorov, A stoichiometric model for sillenites, *Chem. Mater.*, 2002, **14**, 3471–3476.
25 Y. Wang, G. Xu, L. Yang, Z. Ren, X. Wei, W. Weng, *et al.*, Alkali Metal Ions-Assisted Controllable Synthesis of Bismuth Ferrites by a Hydrothermal Method, *J. Am. Ceram. Soc.*, 2007, **90**, 3673–3675.
26 Z. Zheng, J. He, Z. Zhang, A. Kumar, M. Khan, C. W. Lung, *et al.*, Magnetically recyclable nanophotocatalysts in photocatalysis-involving processes for organic pollutant removal from wastewater: current status and perspectives, *Environ. Sci.: Nano*, 2024, **11**, 1784–1816.
27 M. K. Anjiraki, M. Ghiyasiyan-Arani, M. Baladi, F. H. Alsultany, M. Shabani-Nooshabadi and M. Salavati-Niasari, Magnetically recyclable PrFeO3/g-C3N4 nano-photocatalyst with Z-scheme structure: Synthesis and characterization and its application for enhanced degradation of malachite green as contaminated water under sunlight, *Inorg. Chem. Commun.*, 2024, **170**, 113184.
28 F. Samimi and M. Ghiyasiyan-Arani, Zn2Mo3O8/ZnMo8O10/Mo8O23 nanocomposites; structural properties, synthesis and its emerging application in electrochemical hydrogen storage, *Int. J. Hydrogen Energy*, 2024, **91**, 423–433.
29 C. R. Hubbard and R. L. Snyder, RIR-measurement and use in quantitative XRD, *Powder Diffr.*, 1988, **3**, 74–77.
30 G. Wang, D. Cheng, T. He, Y. Hu, Q. Deng, Y. Mao, *et al.*, Enhanced visible-light responsive photocatalytic activity of Bi 25 FeO 40/Bi 2 Fe 4 O 9 composites and mechanism investigation, *J. Mater. Sci.: Mater. Electron.*, 2019, **30**, 10923–10933.
31 K. A. Adegoke and O. S. Bello, Dye sequestration using agricultural wastes as adsorbents, *Water Resour. Ind.*, 2015, **12**, 8–24.
32 A. Jaison, A. Mohan and Y.-C. Lee, Recent Developments in Photocatalytic Nanotechnology for Purifying Air Polluted with Volatile Organic Compounds: Effect of Operating Parameters and Catalyst Deactivation, *Catalysts*, 2023, 407.
33 M. Lyulyukin, N. Kovalevskiy, A. Bukhtiyarov, D. Kozlov and D. Selishchev, Kinetic Aspects of Benzene Degradation over TiO(2)-N and Composite Fe/Bi(2)WO(6)/TiO(2)-N Photocatalysts under Irradiation with Visible Light, *Int. J. Mol. Sci.*, 2023, **24**, 5693.
34 O. Allam, M. Maghsoodi, S. S. Jang and S. D. Snow, Unveiling Competitive Adsorption in TiO(2) Photocatalysis through Machine-Learning-Accelerated Molecular Dynamics, DFT,

and Experimental Methods, *ACS Appl. Mater. Interfaces*, 2024, **16**, 36215–36223.

35 M. Karimi Anjiraki, M. Ghiyasiyan-Arani, Z. Falah Khudair, M. Baladi, M. Shabani-Nooshabadi and M. Salavati-Niasari, A highly efficient PrMnO3/graphene oxide nanocomposite for visible light induced photocatalytic water treatment, *Sol. Energy*, 2024, **275**, 112615.

36 A. Sun, C. Song, F. Jiang and H. Chen, Hydrothermal preparation and visible light photocatalytic activity of Bi25FeO40-graphene nanocomposite, *2013 International Conference on Materials for Renewable Energy and Environment*, 2013, pp. 658–661.